Biosensors and Bioelectronics 165 (2020) 112347

Contents lists available at ScienceDirect

Biosensors and Bioelectronics

journal homepage: http://www.elsevier.com/locate/bios

ZnO-rGO nanocomposite based bioelectrode for sensitive and ultrafast detection of dopamine in human serum

Shilpi Verma [a,b], Priyanshu Arya [c], Anu Singh [d], Jyoti Kaswan [a,b], Ajay Shukla [a,b], Hemant R. Kushwaha [d], Shalini Gupta [c], Surinder P. Singh [a,b,*]

[a] Academy of Scientific and Innovative Research (AcSIR), CSIR-HRDC Campus, Ghaziabad, Uttar Pradesh, 201002, India
[b] CSIR-National Physical Laboratory, Dr. K. S. Krishnan Road, New Delhi, 110012, India
[c] Dept of Chemical Engineering, Indian Institute of Technology Delhi, Hauz Khas, New Delhi, 110016, India
[d] School of Biotechnology, Jawaharlal Nehru University (JNU), New Mehrauli Road, New Delhi, 110067, India

ARTICLE INFO

Keywords:
Reduced graphene oxide
Zinc oxide
Dopamine
Electrochemical biosensor
Nanocomposite
Tyrosinase

ABSTRACT

We present a tyrosinase-conjugated zinc oxide-reduced graphene oxide (Tyr/ZnO-rGO) nanocomposite system as a biosensing test-bed for rapid and sensitive detection of dopamine (DA). The bioelectrodes (Tyr/ZnO-rGO/ITO) were designed by covalently immobilizing tyrosinase enzyme on spin-coated films of ZnO-rGO nanocomposite prepared via self-assembly approach. The cyclic voltammetry (CV) and electrochemical impedance spectroscopy (EIS) showed fast electron transfer kinetics of ZnO-rGO/ITO electrode. The response studies of the Tyr/ZnO-rGO/ITO bioelectrode revealed ultrafast (0.34 ± 0.09 s) detection of DA in a wide linear dynamic range of 0.1–1500 pM. The significant performance of the biosensor in terms of low detection limit (8.75 ± 0.64 pM) and high sensitivity (39.56 ± 0.41 μA nM^{-1}) values is attributed to the fast and unhindered electron transfer mechanism of ZnO-rGO matrix having low electrochemical band gap. The nanoplatform exhibited high selectivity toward DA in human sera, and remained stable up to 3 months at 4 °C, representing its suitability for clinical applications.

1. Introduction

An imbalance in neurotransmitter (NT) concentration may lead to various neurological disorders, therefore reliable detection of NTs is critically important in routine clinical practice (Pearl et al., 2006). Dopamine (DA), belonging to the family of catecholamines, is a major NT that is produced from the decarboxylation of L-dopa in dopaminergic neurons of the basal ganglia in mid brain and the arcuate nucleus present in hypothalamus (Ayano et al., 2016). It regulates various brain functions such as modulation of cognition and behaviour, voluntary actions, mood, sleep, concentration, motivation *etc.* (Calabresi et al., 2007). The dysfunction in dopamine transmission or abnormality in its concentration profile leads to several neurological disorders like depression (Dunlop and Nemeroff, 2007), Parkinson's disease (Höglinger et al., 2004), epilepsy (Starr, 1996) schizophrenia (Brisch et al., 2014) and attention-deficit hyperactivity disorder (ADHD) (Gill et al., 1997). Further, DA is also indirectly involved in regulation of blood pressure, glycogen metabolism, and functions of immune system along with several visceral organs (Olguin et al., 2016). Therefore, the quantitative estimation of DA becomes crucial in monitoring of neurological and other metabolic disorders.

The well-established DA detection methods include capillary-electrophoresis (Zhao et al., 2011), high-performance liquid chromatography (Park et al., 2013), mass spectrometry (El-Beqqali et al., 2007) and fluorescence detection (Qian et al., 2015). Although quite efficient, these methods pose limitations like prolonged detection time, large sample volume, complex sampling, high cost and bulky instrumentation (Wang, 2006a). These limitations can be overcome by using electrochemical biosensors as an alternative to the existing detection methodologies due to their simple preparation, ease of sample handling and capability for faster detection (Ronkainen et al., 2010). However, most of the biosensors developed for direct DA detection, suffer electrode fouling by oxidation products and interference from co-existing biomolecules with similar electroactive potentials (Njagi et al., 2010). Employing DA-specific enzyme as biorecognition unit for analytical detection of enzyme-catalyzed DA oxidation offers promising ability for selective and efficient DA detection (Florescu and David, 2017). Min and Yoo (2009) achieved amperometric detection of DA in the presence of

* Corresponding author. Academy of Scientific and Innovative Research (AcSIR), CSIR-HRDC Campus, Ghaziabad, Uttar Pradesh, 201002, India.
E-mail address: singh.uprm@gmail.com (S.P. Singh).

https://doi.org/10.1016/j.bios.2020.112347
Received 12 February 2020; Received in revised form 29 May 2020; Accepted 31 May 2020
Available online 5 June 2020

ascorbic acid (AA) using Tyrosinase/SWNTs-Ppy electrodes. Maciejewska et al. (2011) used tyrosinase/poly(indole-5-carboxylic acid) modified glassy carbon electrodes for determination of DA in the presence of AA and uric acid (UA). Roychoudhury et al. (2016) recently accounted for the fabrication of tyrosinase/NiO/ITO electrodes that showed high specificity towards DA in the presence of interferents. As mentioned in Table 1, these methods positively contributed towards DA detection but their slow electron transfer rates allowed detection of DA in the micro- and nanomolar ranges only, that are much higher than the physiological range of DA (< 200 pM) in blood plasma (Ambade et al., 2009), thus, making them less feasible for clinical utility.

The sensitivity and efficiency of a biosensor is expected to enhance manifolds by using the right material for transducer matrix. Among the various material systems studied so far (Li et al., 2016; Govindaraju et al., 2017; Thirumalraj et al., 2017), graphene oxide (GO) has been most applied for next generation biosensors due to its atomically thin sheet-like architecture, high surface area, electron transfer capability, biocompatibility and biomolecular affinity. Its amphiphilic nature and functionalities allow facile biomolecular surface modification (Tiwari et al., 2016). The electronic and electrochemical characteristics of GO could be enhanced by altering the number of oxygen functional groups and defects through an appropriate reduction process (Bhardwaj et al., 2016) or by incorporation of metal/metal-oxide nanoparticles (NPs) to improve biosensing capability (Zhou et al., 2009). In this context, direct bandgap semiconductor ZnO (NPs) could be considered beneficial, owing to their facile charge transfer capacity, ample surface area and compatibility with biomolecules (Arya et al., 2012).

We report zinc oxide-reduced graphene oxide (ZnO-rGO) nanocomposites as transducer matrix for sensitive detection of DA. A well-optimized procedure was carried out to prepare ZnO-rGO thin films on indium-tin oxide (ITO) coated glass sheets followed by covalent attachment of tyrosinase (Tyr) enzyme on its surface. The enzyme based bioelectrodes were tested for detection of different concentrations of DA in both standard solutions and serum samples. A detailed schematic of the sensor fabrication and detection process is depicted in Fig. 1. To the best of our knowledge, this is the first report to have investigated the detection of DA in picomolar ranges rendering a detection limit well below its physiological range, that gives it an edge over previously reported biosensors.

2. Materials and methods

All the experiments were performed using chemicals (listed in the supporting information) as received unless otherwise mentioned. The details of the characterization and electrochemical techniques utilized have also been provided in the supporting information.

2.1. Synthesis and characterization of ZnO-rGO nanocomposites

The ZnO-rGO nanocomposites were prepared by self-assembly of ZnO NPs onto GO nanosheets. For this, highly exfoliated GO nanosheets were first prepared using the modified Hummer's process reported elsewhere (Cote et al., 2009; Verma et al., 2017) and the ZnO NPs were synthesized using a sol-gel process (Spanhel and Anderson, 1991). Briefly, 0.7 g of $Zn(OCOCH_3)_2.2H_2O$ was heated at 70 °C in 25 mL of ethanol for 2 h and $LiOH.H_2O$ solution was obtained by sonicating 0.2 g of $LiOH.H_2O$ in 20 mL of ethanol for 1 h. The $LiOH.H_2O$ solution was added to the $Zn(OCOCH_3)_2.2H_2O$ solution at 25 °C under vigorous stirring for 1 h to obtain a clear suspension of ZnO NPs. ZnO-rGO nanocomposites were prepared by mixing 1 mg/mL ethanolic GO solution to 0.6 mL of ZnO NPs suspension. The mixture was allowed to stir overnight for the formation of ZnO-rGO nanocomposite.

2.2. Fabrication of Tyr/ZnO-rGO/ITO bioelectrodes

The synthesized ZnO-rGO nanocomposites were uniformly deposited as thin films on 5 × 10 mm^2 area of pre-cleaned ITO substrates by spin coating at 3000 rpm (Laurell WS-650MZ-23NPP) for 1 min followed by annealing at 100 °C for 3 h. A 50 μL solution of 1:1(v/v) EDC(0.5M):NHS (0.1 M) was drop casted onto 5 × 6 mm^2 of the ZnO-rGO/ITO surface and left for 15 min to activate the carboxylic groups in the ZnO-rGO nanocomposite. The activated films were then incubated with 20 μL of 10 units/μL tyrosinase (prepared in 50 mM PBS) for 4 h to allow its effective covalent binding on the film surface. The films were washed with 50 mM PBS (pH 7.2) solution to remove the unattached enzyme and treated with 1 M ethanolamine to block the unbound active sites resulting into the desired Tyr/ZnO-rGO/ITO bioelectrodes.

3. Results and discussion

The efficient electrode kinetics leading to selective DA detection in

Table 1
Comparison of analytical parameters obtained for electrochemical detection of DA in earlier reports with the present study.

S. N.	Matrix	Immobilization strategy	Linear dynamic range	Sensitivity	LOD	Time (s)	Technique	Ref.
1.	Pristine SWCNTs network electrode	Direct	100 nM and 500 nM	–	–	–	CV	Bertoncello et al. (2007)
2.	Tyrosinase/SWNTs–Ppy	Enzymatic (covalently attached)	5–50 μM	467 mA/M cm^2	5 μM	<5	Amperometry	Min and Yoo (2009)
3.	EDTA-reduced Graphene/ nafion/GC	Direct	0.2–25 μM	–	0.01 μM	-	DPV	Hou et al. (2010)
4.	MWCNTs/GONRs/GC	Direct	0.15–12.15 μM	–	0.08 μM	2.125	Amperometry	Sun et al. (2011)
5.	Tyrosinase/poly(indole-5-carboxylic acid)/GC	Enzymatic (covalently attached)	0.5–20 μM	6.2 A/M cm^2 with UA & 2.3 A/M cm^2 with AA	0.1–0.5 μM	–	Amperometry	Maciejewska et al. (2011)
6.	GO-Ag/Poly-L-Lysine/GC	Direct	0.1–10 μM	1.48 μA/μM	0.03 μM	–	DPV	Guo et al. (2015)
7.	Tyrosinase/NiO/ITO	Physical	2–100 μM	60.2 nA μM^{-1}	1.038 μM	45	CV	Roychoudhury et al. (2016)
8.	Carbon paste electrode/GO	Direct	0.08–2.30 μM	-	8.60 nM	-	DPV	Ghoreishi et al. (2016)
9.	Gallic acid-RGO/AuNPs	Direct	0.01–100.3 μM	3.58 μA μM^{-1} cm^{-2}	2.6 nM	–	DPV	Thirumalraj et al. (2017)
10.	GO-ionic liquid-AuNPs/GC	Direct	7 nM-5 μM	–	2.3 nM	–	DPV	Li et al. (2017)
11.	Poly(3,4-ethylenedioxythiophene)/rGO/GC	Direct	19.6–122.8 μM	3.27 μA μM^{-1} cm^{-2}	1.92 μM	–	DPV	Cogal et al. (2018)
12.	Tyrosinase/ZnO-rGO/ITO	Enzymatic (covalently attached)	0.1–1500 pM	39.56 ± 0.41 μA nM^{-1}	8.75 ± 0.64 pM	0.34 ± 0.09	DPV	Present Study

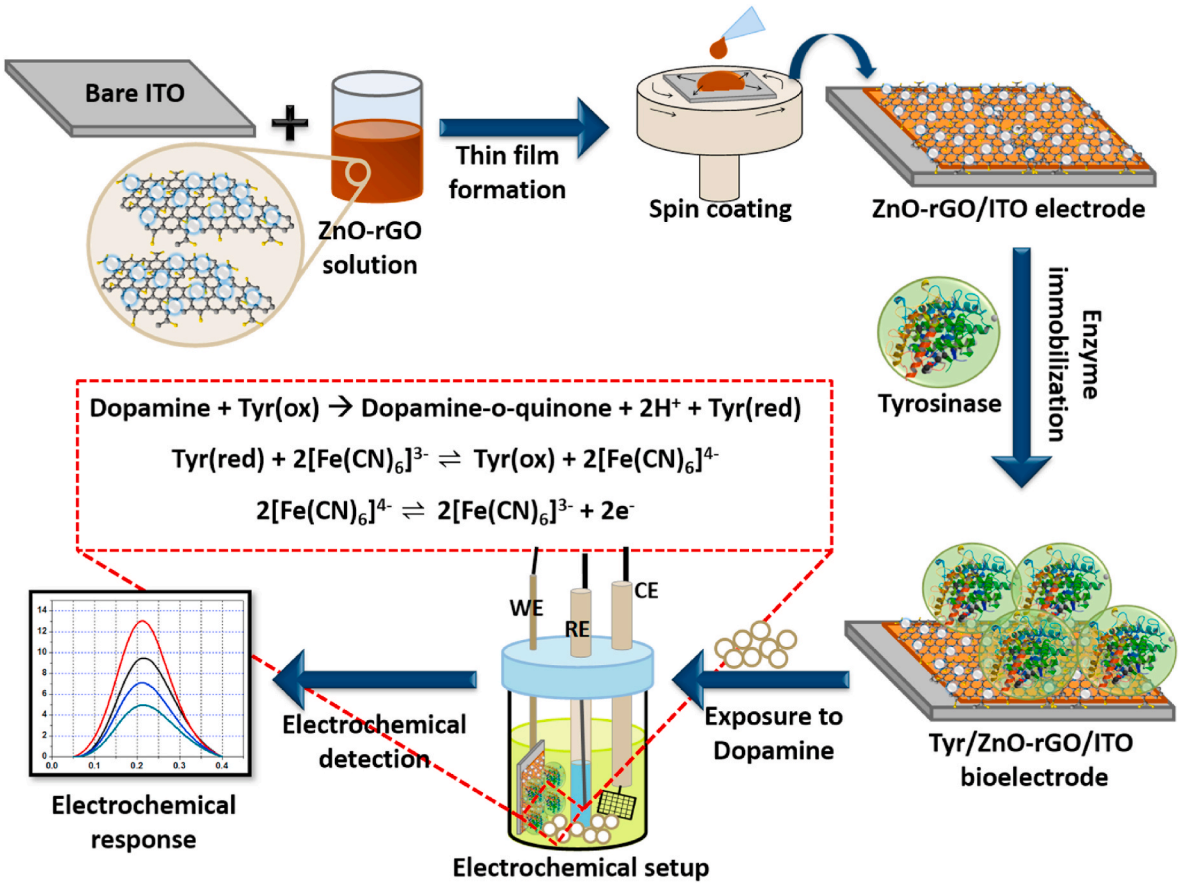

Fig. 1. Schematic representation of the fabrication and working of Tyr/ZnO-rGO/ITO biosensing platform.

the pM range was achieved by incorporating ZnO NPs (IEP ~ 9.4) onto rGO sheets that provided faster electron mobility and biochemical stability to the tyrosinase enzyme immobilized on the electrode surface. The combined structural and electrochemical properties of ZnO-rGO made the system more susceptible to changes in its local environment, allowing more effective biosensing. The coming sections give the detailed information on bioelectrode fabrication, characterization and DA detection.

3.1. Characterization of ZnO-rGO nanocomposites

The successful formation of ZnO-rGO nanocomposite was corroborated using x-ray diffraction (XRD), ultraviolet-visible (UV–Vis) spectroscopy, Raman and transmission electron microscopy (TEM) studies, that have been discussed in the supporting information (see Figs. S1 and S2) and matched well with our previous studies (Verma and Singh, 2019). This section gives the elemental and chemical state analysis of ZnO-rGO nanocomposite through x-ray photoelectron spectroscopy (XPS) studies. The XPS survey spectra for GO, ZnO NPs, ZnO-rGO samples over a wide binding energy (BE) range is shown in Fig. S3 of supporting information. The C 1s core level spectra for GO, ZnO-rGO and Tyr/ZnO-rGO along with fitting components are shown in Fig. 2a. For GO, five nearly Gaussian peaks, centred at 284.5 (C═C/C–C), 285.9 (C–OH), 286.8 (C–O), 287.5 (C═O) and 288.4 (-COOH) eV BE, have been used to fit C 1s core level (Verma et al., 2017; Datsyuk et al., 2008; Kumar et al., 2015, Liu et al., 2018). For ZnO-rGO, a significant decrease in the C–O and increase in C–OH compared to GO was observed, along with appearance of two additional components centred at 290.1 (O–C═O) and 291.4 (carbonate) eV BE (Datsyuk et al., 2008; Kumar et al., 2015, Liu et al., 2018). The C 1s core level of Tyr/ZnO-rGO showed an additional component at lower BE side which was ascribed to C–Na coming from the chelation of Na ions in PBS (used for tyrosinase preparation) with the enzyme carbon atoms. Fig. 2b shows Zn 2p core level spectra for ZnO NPs and ZnO-rGO nanocomposite. For ZnO NPs, observed BE positions and spin-orbit splitting of Zn $2p_{3/2}$ (1021.4 eV) and Zn $2p_{1/2}$ (1044.5 eV) doublet were close to characteristic values of Zn^{2+} in ZnO (Liu et al., 2018; Pradhan and Leung, 2008; Yuan et al., 2016; Kim et al., 2017). Additional features at higher BE side, observed for ZnO-rGO nanocomposite, is attributed to $Zn(OH)_2$ formation on the surface of composite (Pradhan and Leung, 2008). Interestingly, a shift in Zn 2p core level of ZnO-rGO nanocomposite towards higher BE side by 0.8 eV compared to ZnO NPs was observed. Such shift has also been observed in other ZnO containing composites and can be taken as clear evidence of electronic interaction/charge transfer between ZnO NPs and rGO (Liu et al., 2018; Yuan et al., 2016; Kim et al., 2017).

3.2. Electrochemical studies on ZnO-rGO/ITO electrodes

The electrochemical activity of ZnO-rGO/ITO was measured via CV in 3 mM Zobell's solution at varying scan rates within the range 0.01–0.15 Vs^{-1}. The results showed that with increase in scan rate, both the redox peak currents (I_{pa} and I_{pc}) and the peak separation potential ($\Delta E_p = E_{pa} - E_{pc}$) of the ferro-ferri couple at ZnO-rGO/ITO electrode increased (Fig. 3a), indicating Nernstian behaviour with quasi-reversible electron-transfer kinetics. The quasi-reversible regime was also proved by the I_{pa}/I_{pc} ratio that lay in the 1.10–1.17 range (Wang, 2006b). Further, the anodic (I_{pa}) and cathodic (I_{pc}) peak currents exhibited linear dependence on the square roots of scan rates (Fig. 3b), suggesting the redox process at the electrode surface to be dominantly diffusion-controlled. Using the Randles-Sevcik equation (eq. (1)) (Bard and Faulkner, 2001), the electrochemical diffusion coefficient (D) was determined to be 1.74×10^{-5} cm^2 s^{-1}.

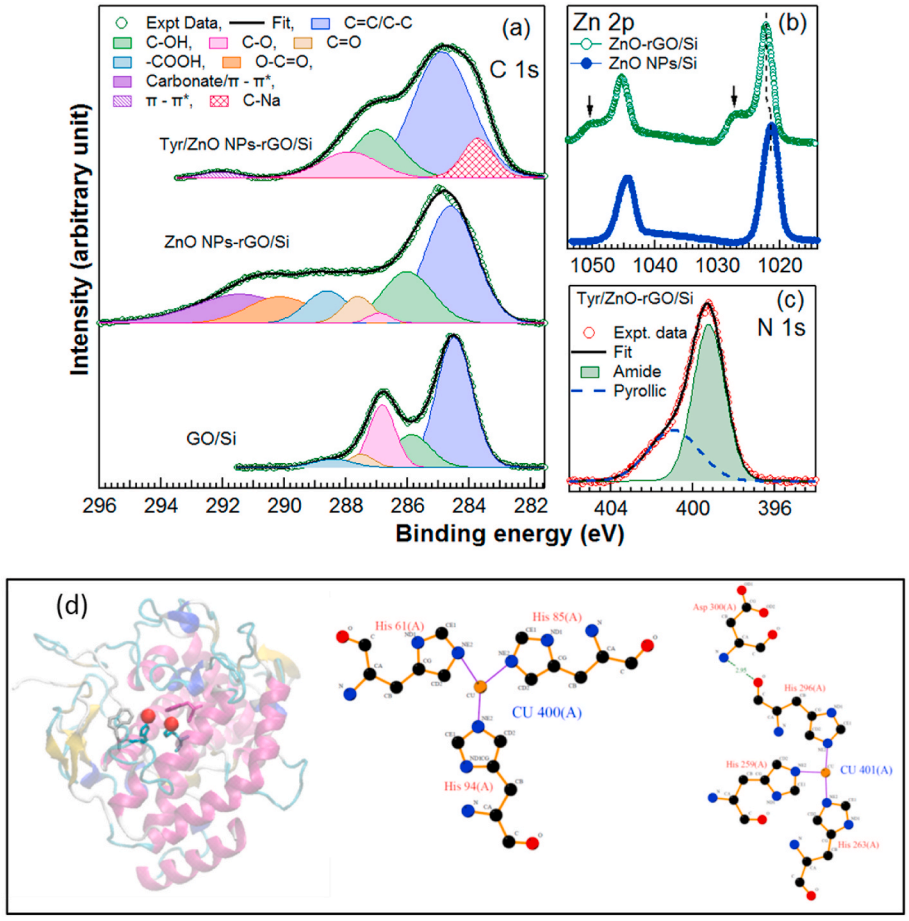

Fig. 2. (a) C 1s core level spectra (open circles) for GO, ZnO-rGO and Tyr/ZnO-rGO samples. Fitted data (solid line) and deconvoluted fitting components (shaded and patterned regions) are also shown; **(b)** Zn 2p core level spectra for ZnO NPs and ZnO-rGO; **(c)** N 1s core level for Tyr/ZnO-rGO. All the spectra have been normalized to have same peak height at the highest peak for ease of comparison. **(d)** 3D structure (using VMD) of Tyrosinase enzyme of Agaricus bisporus showing a tetramer complex comprising of two H subunits of ~392 residues and two L subunits of ~150 residues. The H subunit contains a binuclear copper-binding site in the deoxy-state, in which three histidine residues coordinate each copper ion. The side chains of these histidines have their orientation fixed by hydrogen bonds or, in the case of His85, by a thioether bridge with the side chain of Cys83.

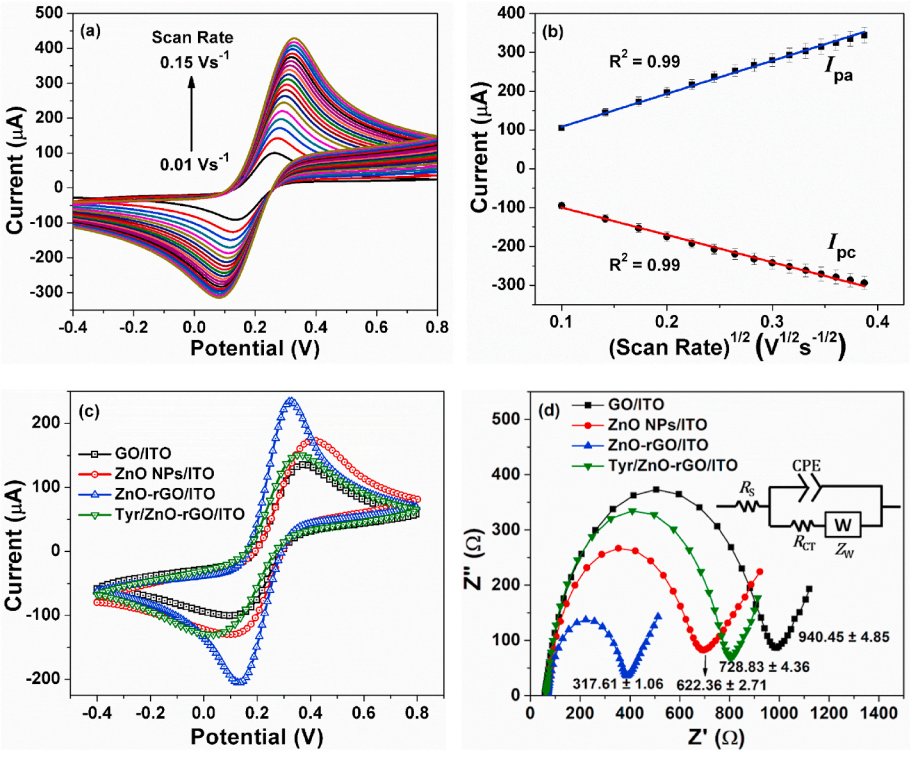

Fig. 3. (a) CV curves recorded at ZnO-rGO/ITO electrode in 3 mM Zobell's solution at scan rates ranging from 0.01 to 0.15 Vs^{-1}. **(b)** Plot showing variation of anodic (I_{pa}) and cathodic (I_{pc}) peak currents with respect to square root of scan rate values. Surface modification of electrodes after each modification step studied by **(c)** CV curves recorded at scan rate of 0.05 Vs^{-1} and **(d)** Nyquist plots recorded at potential 0.2 V with frequency range of 0.1 Hz–100 kHz, in 3 mM Zobell's solution. **(d)-Inset:** Schematic diagram of Randles electronic circuit.

$$I_p = \left(2.69 \times 10^5\right) n^{3/2} A\, C\, D^{1/2} \nu^{1/2} \quad \text{eq. 1}$$

Here, I_p is the anodic/cathodic peak current (in amperes), n is the number of electrons involved in the redox process, A is the active surface area of the electrodes (in cm^2), C is the molar concentration of the redox species (in $mol.cm^{-3}$) and ν is the applied scan rate (in Vs^{-1}).

Nicholson's method (Nicholson, 1965) was applied to estimate the standard heterogeneous rate constant (k°) using eq. (2),

$$\psi = k^o \left[\pi D n \nu F/RT\right]^{-1/2} \quad \text{eq. 2}$$

where, ψ is the Nicholson's kinetic parameter dependent on ΔE_p, n is the number of electrons transferred in the oxidation/reduction process (here, $n = 1$), F is the Faraday constant, R is the universal gas constant and T is the temperature (in Kelvin). Values of ψ were determined for every scan rate in the range 0.01–0.15 Vs^{-1} from Lavagnini's equations (Lavagnini et al., 2004) where, ψ varied linearly with $[\pi D n \nu F/RT]^{-1/2}$ (Fig. S4, supporting information). The value of k° was obtained to be 1.76×10^{-3} cm s^{-1} from the slope of ψ *vs* $[\pi D n \nu F/RT]^{-1/2}$ plot.

Further, the change in electrochemical activities of the electrodes after every modification step was explored by CV where the redox curves for 3 mM Zobell's solution were obtained at a fixed scan rate of 0.05 Vs^{-1} (Fig. 3c). The CV curves clearly indicated that GO/ITO exhibited low redox current as compared to ZnO NPs/ITO electrode. The enhancement in redox current for ZnO NPs/ITO electrode may be due to direct bandgap and high electron transfer capability of ZnO NPs (Arya et al., 2012). On the other hand, ZnO-rGO/ITO electrode featured superior electron transfer than both GO/ITO and ZnO NPs/ITO electrodes as evident from its high redox current and low peak separation potential (Table T1-supporting information). This enhancement could be attributed to the overall reduction in the electrochemical bandgap of the nanocomposite in comparison to its precursors, that plays a vital role in facilitating facile and improved electron mobility across its surface. The bandgap values obtained from CV are as follows: 3.20 eV (GO/ITO), 3.75 eV (ZnO NPs/ITO), and 2.21 eV (ZnO-rGO/ITO) (see Fig. S5, supporting information for details).

To further corroborate the observed variation in electron transfer kinetics for the above mentioned three electrodes along with enzyme modified electrode, EIS measurements were carried out in 3 mM Zobell's solution. Nyquist plots (Fig. 3d) consisting of imaginary part (Z'') versus real part (Z') were simulated according to the Randles equivalent circuit model shown in Fig. 3d-inset. The circuit consists of the R_S component which is the ohmic resistance from the solution, in series with the combination of constant phase element (CPE) parallelly combined with the charge transfer resistance (R_{CT}) of the Faradaic process and the Wargburg impedance (Z_W) component arising from the mass diffusion towards the electrode surface. Herein, the CPE component is incorporated instead of the true double layer capacitance (C_{dl}) due to heterogeneity in the electrode surface that contributes to the imperfect capacitance. The obtained R_{CT} values corresponding to the Faradaic process taking place at various modified electrodes are given in Fig. 3d and in Table T1-supporting information. A notably small R_{CT} value was obtained in case of ZnO-rGO/ITO electrode in comparison to others, advocating its expeditious electron transfer capabilities and potential as an efficient transducer matrix.

3.3. Enzyme immobilization and response studies of Tyr/ZnO-rGO/ITO

Once the electrode surface was fully characterized, the EDC-NHS chemistry was used to covalently bind the tyrosinase enzyme to the ZnO-rGO/ITO electrodes through amide linkages between the amine groups in the enzyme and the carboxylic groups on rGO. FTIR measurements confirmed the successful immobilization of enzyme as evident from the appearance of peaks corresponding to the stretching frequencies (3352 cm^{-1} N–H, 1637 cm^{-1} amide C═O, 1267 cm^{-1} C–N) of the amide group functionalities in the enzyme (Fig. S6, supporting information). The tyrosinase immobilization on the ZnO-rGO film surface was also further confirmed from the XPS survey spectrum (Fig. S3 in supporting information) and N 1s core level spectrum of Tyr/ZnO-rGO (Fig. 2c). N 1s signal observed for Tyr/ZnO-rGO sample has been fitted with two components. BE position of the main N 1s peak is found to be 399.3 eV, which is close to the expected BE value for amide (NH–C═O) (Verma et al., 2017; Stathi et al., 2015). It evidences attachment of tyrosinase to ZnO-rGO nanocomposite. Higher BE N 1s component (400.1 eV) can be linked to pyrrolic-N in histidine molecules of tyrosinase enzyme (Fig. 2d) (Stathi et al., 2015).

Further, the reduction in redox current after tyrosinase immobilization due to the slow electrode kinetics offered by the non-conducting layer of the enzyme on the electrode surface corroborates the presence of tyrosinase (Fig. 3c). Correspondingly, the Tyr/ZnO-rGO/ITO bioelectrode also exhibited a higher R_{CT} value, a signature of the sluggish electron transfer process as a result of tyrosinase immobilization (Fig. 3d).

The electrochemical response of Tyr/ZnO-rGO/ITO was investigated using a more sensitive technique *i.e.,* differential pulse voltammetry (DPV). In this, the bioelectrode response was first optimized in terms of the experimental parameters that govern the efficient detection of DA. The working pH and enzyme loading were optimized, and are given in supporting information (see Fig. S7) in detail. The pH of 6.9 as working pH and enzyme concentration of 200 U for immobilization were chosen after optimization for designing the biosensor for effective detection of DA.

Once the experimental conditions were optimized, the bioelectrodes were exposed to different concentrations of DA (0.1–1500 pM) and the oxidation reaction was monitored through the electrochemical response recorded using DPV technique in 3 mM Zobell's solution. As evident from Fig. 4a, clear distinct oxidation peaks were obtained at 0.226 ± 0.007 V for all the exposed concentrations of DA as a result of facile electron transport facilitated by ZnO-rGO nanocomposite. The mediator assisted tyrosinase catalyzed oxidation reaction of DA (depicted in the following reaction sequence), served as the channel for availability of electrons at the bioelectrode surface causing increase in oxidation current with increase in DA concentration.

$$\text{Dopamine} + \text{Tyr(ox)} \rightarrow \text{Dopamine} - \text{o} - \text{quinone} + 2H^+ + \text{Tyr(red)}$$

$$\text{Tyr(red)} + 2\left[Fe(CN)_6\right]^{3-} \rightleftharpoons \text{Tyr(ox)} + 2\left[Fe(CN)_6\right]^{4-}$$

$$2\left[Fe(CN)_6\right]^{4-} \rightleftharpoons 2\left[Fe(CN)_6\right]^{3-} + 2e^-$$

The reactions show that the enzymatic oxidation of DA leads to simultaneous reduction of the tyrosinase enzyme. The enzyme regeneration after DA oxidation is then accomplished by reduction of $[Fe(CN)_6]^{3-}$ (ferricyanide ions) that act as a mediator for scavenging electrons from the enzyme's active site and themselves get reduced to $[Fe(CN)_6]^{4-}$ (ferrocyanide ions) increasing the amount of the latter at the bioelectrode surface. The oxidation of the accumulated ferrocyanide ions to ferricyanide ions caused by the applied potential gives the analytical signal corresponding to DA concentration. A calibration curve for the obtained oxidation current values with respect to exposed DA concentrations showed a linear trend with a regression coefficient of 0.99 (Fig. 4b). The slope of the calibration curve gave the sensitivity of the fabricated biosensor as 39.56 ± 0.41 μA nM^{-1} and the lower limit of detection (LOD) was estimated as 8.75 ± 0.64 pM from eq. (3) (Tiwari et al., 2016; Miller and Miller, 2010),

$$LOD = k \times \sigma/S \quad \text{eq. 3}$$

Here, k (= 3 at statistical confidence of 99.6%) is the confidence level parameter, σ is the standard deviation of the current values for control sample and S is the sensitivity obtained from slope of the calibration curve. This obtained LOD is significantly lower than other enzyme-based and direct electrochemical biosensors reported in the literature (see

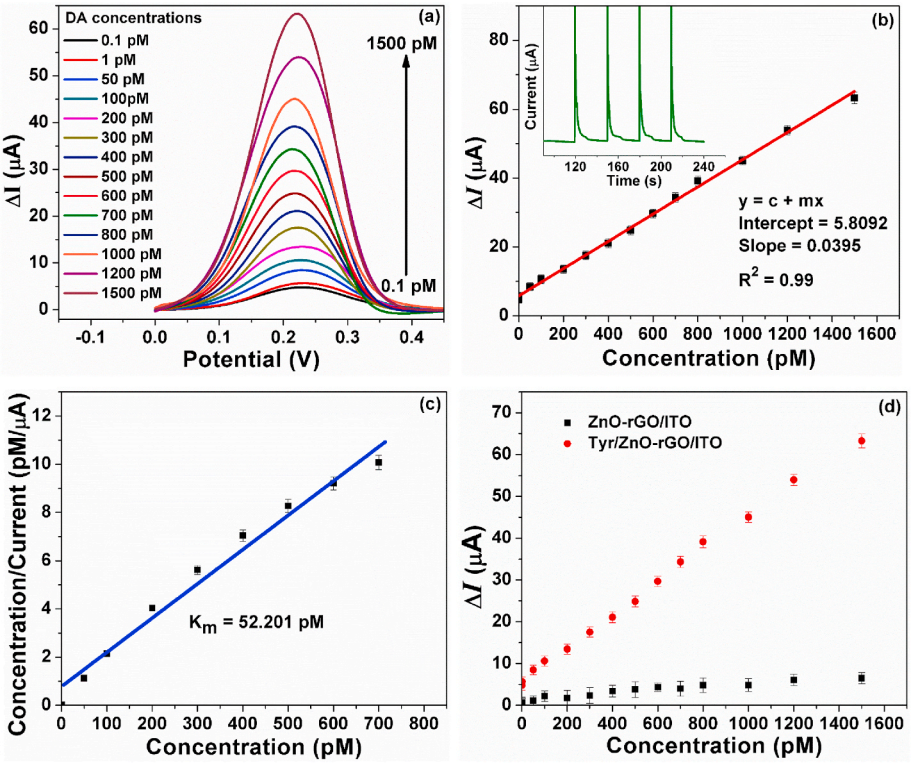

Fig. 4. (a) DPV response of Tyr/ZnO-rGO/ITO bioelectrodes towards different DA concentrations. **(b)** Calibration curve plotted between DPV response current and exposed DA concentrations. **(b)-Inset**: Current vs time plot showing chronoamperometric response of Tyr/ZnO-rGO/ITO bioelectrode towards DA. **(c)** Hanes plot to determine the Michaelis-Menten constant (K_m) associated with enzyme activity. **(d)** Comparison of responses between ZnO-rGO/ITO and Tyr/ZnO-rGO/ITO electrodes towards different DA concentrations.

Table 1).

Chronoamperometry measurements were performed to determine the response time of the fabricated biosensor. The sensor showed an instant response within 0.34 ± 0.09 s in terms of signal enhancement on each addition of DA, thus demonstrating its ultrafast response mechanism as shown in Fig. 4b-inset. Further, the Michaelis-Menten constant (K_m) value of 52.20 pM for immobilized tyrosinase enzyme was determined by Hanes plot (Fig. 4c) indicating high affinity of tyrosinase enzyme towards DA. In addition, control experiments performed in the absence of enzyme (Fig. 4d) and/or mediator (Fig. S8, supporting information) showed feeble and erratic trends, respectively, establishing the important role of these molecules in the biosensing process of the fabricated biosensor.

3.4. Selectivity, shelf-life and reusability studies

To ensure that the fabricated biosensor does not give false positives on exposure to other biomolecules, we recorded the selectivity of our sensor by measuring its analytical response in presence of different analytes like glucose (glu), UA, AA and serotonin that co-exist with DA in biological fluids (Fig. 5a). The interference from these analytes was estimated from the selectivity coefficient, k_{sel}, that was determined using eq. (4) (Verma et al., 2019).

$$k_{sel} = (Signal)_{interferent} / (Signal)_{DA} \quad \text{eq. 4}$$

In all the cases, the estimated k_{sel} values were found to be significantly low i.e. « 1 (see Fig. 5a-inset) suggesting minimal effect of these molecules on the biosensor response. The shelf-life of the sensor was determined by recording the response of three sets of bioelectrodes towards 300 pM DA after every 15 days duration (Fig. 5b). Our results showed that when stored at 4 °C, the biosensor remained stable up to 3 months with RSD <4.2% ($n = 3$). Furthermore, significant reusability of the biosensor was seen as it exhibited > 90% response for up to 54 cycles (RSD < 3.1%) when exposed to 300 pM DA (Fig. 5c).

3.5. Real sample analysis

The clinical utility of the biosensor was demonstrated by repeating the experiments in spiked serum samples. For this purpose, human serum obtained from blood bank was diluted 20 times with Zobell's solution and spiked with different amounts of DA. The responses of the biosensor towards spiked DA samples were then recorded using DPV and compared with the results obtained for standard solutions of DA shown in section 3.3. The % recovery values of the spiked DA samples calculated using eq. (5) (Verma et al., 2019) were found to lie in the range of 89–96% (see Fig. S9 and Table T3, supporting information) indicating insignificant impact of test-sample matrix on the sensor response.

$$\%\ Recovery = \frac{C_i - C_o}{C_x} \times 100 \quad \text{eq. 5}$$

Here, C_i and C_o are the experimentally obtained concentrations of DA in spiked and unspiked serum samples, and C_x is the concentration of DA actually spiked into the serum samples. Thus, detailed characterization and response studies show that our sensor is highly suitable for reliable and sensitive detection of DA in biological samples.

4. Conclusions

We have successfully demonstrated a highly sensitive and robust electrochemical biosensing platform for efficient detection and quantification of DA using tyrosinase immobilized ZnO-rGO nanocomposites onto ITO electrodes. The nanocomposite matrix comprising of 4–6 nm ZnO NPs uniformly embedded on rGO sheets allowed efficient charge transfer. At an optimum pH of 6.9 and tyrosinase loading capacity of 200 U, the assay displayed a wide dynamic range of 0.1–1500 pM with a high sensitivity of 39.56 ± 0.41 μA nM^{-1} and LOD as low as 8.75 ± 0.64 pM. This LOD is by far the lowest reported for electrochemical detection of DA. The response time of the sensor was only 0.34 ± 0.09 s and it was highly selective for DA in a wide range of components found in the blood serum. The shelf-life of the sensor was approx. 3 months and it could be used for > 50 times while retaining up to 90% activity. The % DA

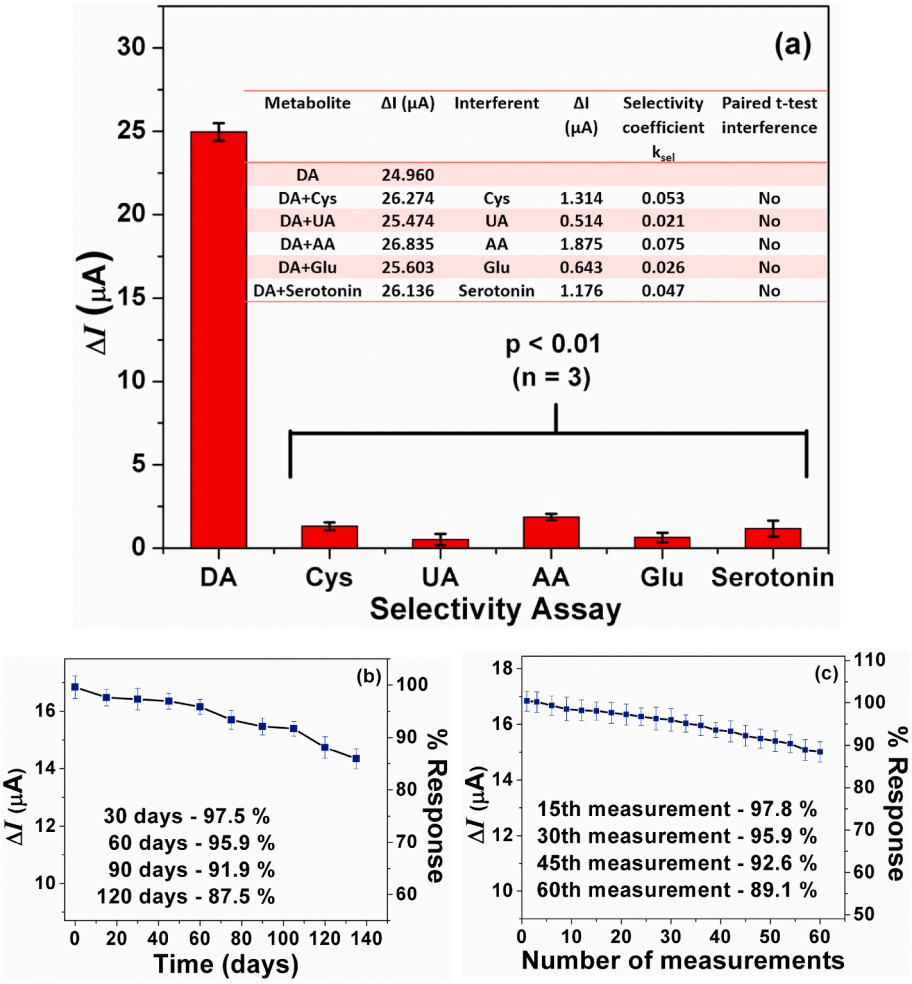

Fig. 5. **(a)** Bar graph depicting current response of Tyr/ZnO-rGO/ITO bioelectrode towards non-target analytes. **(a)-Inset:** Statistical evaluation of interferents on the biosensor performance determined by selectivity coefficient and *t*-test. Graphs showing variation in Tyr/ZnO-rGO/ITO bioelectrode response towards DA **(b)** over a time period of 135 days and **(c)** after many subsequent measurements.

recovery in spiked serum samples was found to be close to 90% establishing the high diagnostic potential of our biosensing system for clinical diagnosis of neuronal disorders.

Declaration of competing interest

The authors declare that they have no known competing financial interests or personal relationships that could have appeared to influence the work reported in this paper.

CRediT authorship contribution statement

Shilpi Verma: Investigation, Methodology, Writing - original draft, Formal analysis, Data curation, Visualization. **Priyanshu Arya:** Investigation. **Anu Singh:** Validation, Methodology, Writing - review & editing. **Jyoti Kaswan:** Formal analysis. **Ajay Shukla:** Resources, Formal analysis. **Hemant R. Kushwaha:** Software. **Shalini Gupta:** Validation, Writing - review & editing, Resources, Project administration, Funding acquisition. **Surinder P. Singh:** Supervision, Conceptualization, Validation, Writing - review & editing, Data curation, Resources, Funding acquisition.

Acknowledgements

We acknowledge Director NPL for providing the lab facilities to carry out this experiment. SV sincerely acknowledges the funding from CSIR (31/01/(0510)/2018-EMR-1). AS gratefully acknowledges the funding assistance from UGC (F.15-1/2016-17/PDFWM-2015-17-UTT-33566 (SA-II)). SG acknowledges DBT NE-Twinning Program (BCIL/NER-BPMC/2016) for financial support. SPS acknowledges BSC0112 network project from CSIR for funding and research facilities.

Appendix A. Supplementary data

Supplementary data to this article can be found online at https://doi.org/10.1016/j.bios.2020.112347.

References

Ambade, V., Arora, B.M.M., Singh, P., Somani, B.L., Basannar, D., 2009. MJAFI (Med. J. Armed Forces India) 65, 216–220.
Arya, S.K., Saha, S., Ramirez-Vick, J.E., Gupta, V., Bhansali, S., Singh, S.P., 2012. Anal. Chim. Acta 737, 1–21.
Ayano, G., 2016. J. Ment. Disord. Treat. 2, 120.
Bard, A.J., Faulkner, L.R., 2001. Electrochemical Methods Fundamentals and Applications, second ed. John Wiley and Sons, Inc., New York.
Bertoncello, P., Edgeworth, J.P., Macpherson, J.V., Unwin, P.R., 2007. J. Am. Chem. Soc. 129, 10982–10983.
Bhardwaj, S.K., Yadav, P., Ghosh, S., Basu, T., Mahapatro, A.K., 2016. ACS Appl. Mater. Interfaces 8, 24350–24360.
Brisch, R., Saniotis, A., Wolf, R., Bielau, H., Bernstein, H.-G., Steiner, J., Bogerts, B., Braun, K., Jankowski, Z., Kumaratilake, J., Henneberg, M., Gos, T., 2014. Front. Psychiatr. 5, 47.
Calabresi, P., Picconi, B., Tozzi, A., Di Fillipo, M., 2007. Trends Neurosci. 30, 211–219.

Cogal, S., 2018. Anal. Lett. 51, 1666–1679.
Cote, L.J., Kim, F., Huang, J., 2009. J. Am. Chem. Soc. 131, 1043–1049.
Datsyuk, V., Kalyva, M., Papagelis, K., Parthenios, J., Tasis, D., Siokou, A., Kallitsis, I., Galiotis, C., 2008. Carbon 46, 833–840.
Dunlop, B.W., Nemeroff, C.B., 2007. Arch. Gen. Psychiatr. 64, 327–337.
El-Beqqali, A., Kussak, A., Abdel-Rehim, M., 2007. J. Separ. Sci. 30, 421–424.
Florescu, M., David, M., 2017. Sensors 17, 1314.
Ghoreishi, S.M., Behpour, M., Mortazavi, M., Khoobi, A., 2016. J. Mol. Liq. 215, 31–38.
Gill, M., Daly, G., Heron, S., Hawi, Z., Fitzgerald, M., 1997. Mol. Psychiatr. 2, 311–313.
Govindaraju, S., Ankireddy, S.R., Viswanath, B., Kim, J., Yun, K., 2017. Sci. Rep. 7, 40298.
Guo, Z., Huang, G.-Q., Li, J., Wang, Z.-Y., Xu, X.-F., 2015. J. Electroanal. Chem. 759, 113–121.
Höglinger, G.U., Rizk, P., Muriel, M.P., Duyckaerts, C., Oertel, W.H., Caille, I., Hirsch, E. C., 2004. Nat. Neurosci. 7, 726–735.
Hou, S., Kasner, M.L., Su, S., Patel, K., Cuellari, R., 2010. J. Phys. Chem. C 114, 14915–14921.
Kim, M.Y., Naveen, M.H., Gurudatt, N.G., Shim, Y.B., 2017. Small 13, 1700502.
Kumar, N., Srivastava, A.K., Patel, H.S., Gupta, B.K., Varma, G.D., 2015. Eur. J. Inorg. Chem. 2015, 1912–1923.
Lavagnini, I., Antiochia, R., Magno, F., 2004. Electroanalysis 16, 505–506.
Li, J., Wang, Y., Sun, Y., Ding, C., Lin, Y., Sun, W., Luo, C., 2017. RSC Adv. 7, 2315–2322.
Li, Y., Jiang, Y., Mo, T., Zhou, H., Li, Y., Li, S., 2016. J. Electroanal. Chem. 767, 84–90.
Liu, C., Yue, M., Liu, L., Rui, Y., Cui, W., 2018. RSC Adv. 8, 22402–22410.
Maciejewska, J., Pisarek, K., Bartosiewicz, I., Krysinski, P., Jackowska, K., Biegunski, A. T., 2011. Electrochim. Acta 56, 3700–3706.
Miller, J.N., Miller, J.C., 2010. Statistics and Chemometrics for Analytical Chemistry, sixth ed. Pearson Education Limited, England.
Min, K., Yoo, Y.J., 2009. Talanta 80, 1007–1011.
Nicholson, R.S., 1965. Anal. Chem. 37, 1351–1355.
Njagi, J., Chernov, M.M., Leiter, J.C., Andreescu, S., 2010. Anal. Chem. 82, 989–996.
Olguín, H.J., Guzmán, D.C., García, E.H., Mejía, G.B., 2016. Oxid. Med. Cell. Longev. 2016, 9730467.
Park, J.Y., Myung, S.W., Kim, I.S., Choi, D.K., Kwon, S.J., Yoon, S.H., 2013. Biol. Pharm. Bull. 36, 252–258.
Pearl, P.L., Hartka, T.R., Taylor, J., 2006. Curr. Treat. Options Neurol. 8, 441–450.
Pradhan, D., Leung, K.T., 2008. J. Phys. Chem. C 112, 1357–1364.
Qian, C.G., Zhu, S., Feng, P.J., Chen, Y.L., Yu, J.C., Tang, X., Liu, Y., Shen, Q.D., 2015. ACS Appl. Mater. Interfaces 7, 18581–18589.
Ronkainen, N.J., Halsall, H.B., Heineman, W.R., 2010. Chem. Soc. Rev. 39, 1747–1763.
Roychoudhury, A., Basu, S., Jha, S.K., 2016. Biosens. Bioelectron. 84, 72–81.
Spanhel, L., Anderson, M.A., 1991. J. Am. Chem. Soc. 113, 2826–2833.
Starr, M.S., 1996. Synapse 22, 159–194.
Stathi, P., Gournis, D., Deligiannakis, Y., Rudolf, P., 2015. Langmuir 31, 10508–10516.
Sun, C.-L., Chang, C.-T., Lee, H.-H., Zhou, J., Wang, J., Sham, T.-K., Pong, W.-F., 2011. ACS Nano 5, 7788–7795.
Thirumalraj, B., Rajkumar, C., Chen, S.-M., Palanisamy, S., 2017. Sci. Rep. 7, 41213.
Tiwari, J.N., Vij, V., Kemp, K.C., Kim, K.S., 2016. ACS Nano 10, 46–80.
Verma, S., Choudhary, J., Singh, K.P., Chandra, P., Singh, S.P., 2019. Int. J. Biol. Macromol. 130, 333–341.
Verma, S., Singh, A., Shukla, A., Kaswan, J., Arora, K., Ramirez-Vick, J., Singh, P., Singh, S.P., 2017. ACS Appl. Mater. Interfaces 9, 27462–27474.
Verma, S., Singh, S.P., 2019. MRS Commun 9, 1227–1234.
Wang, J., 2006a. Biosens. Bioelectron. 21, 1887–1892.
Wang, J., 2006b. Analytical Electrochemistry, third ed. John Wiley and Sons, New Jersey.
Yuan, X., Zhou, C., Jing, Q., Tang, Q., Mu, Y., Du, A., 2016. Nanomaterials 6, 173.
Zhou, X., Huang, X., Qi, X., Wu, S., Xue, C., Boey, F.Y.C., Yan, Q., Chen, P., Zhang, H., 2009. J. Phys. Chem. C 113, 10842–10846.
Zhao, Y., Zhao, S., Huang, J., Ye, F., 2011. Talanta 85, 2650–2654.